Large-eddy simulation of a spatially-evolving supersonic turbulent boundary layer at $M_\infty = 2$

M.S. Shadloo[a], A. Hadjadj[a,*], O. Ben-Nasr[a], A. Chaudhuri[b]

[a] *CORIA-UMR 6614, Normandie University, CNRS-University & INSA, 76000 Rouen, France*
[b] *Department of Aerospace Engineering and Engineering Mechanics, San Diego State University, 5500 Campanile Drive, San Diego, CA, 92182 USA*

Abstract

The ability of large-eddy simulation (LES) to resolve the most energetic coherent structures of a spatially-evolving supersonic turbulent boundary layer over a flat plate at $M_\infty = 2$ and $Re_\theta \approx 6000$ is analyzed using three types of local subgrid scale models. Aditionally, an Implicit LES (ILES), which relies on the intrinsic numerical dissipation to act as a subgrid model, is investigated to assess the consistency and the accuracy of the method. Direct comparison with data from high resolution DNS calculations [*S. Pirozzoli and M. Bernardini, Turbulence in supersonic boundary layers at moderate Reynolds number, J. Fluid Mech, 68, 120-168, 2011*] provides validation of the different modeling approaches. Turbulence statistics up to the fourth-order are reported, which helps emphasizing some salient features related to near-wall asymptotic behavior, mesh resolution and models prediction. Detailed analysis of the near-wall asymptotic behavior of all relevant quantities shows that the models are able to correctly reproduce the near-wall tendencies. The thermodynamic fluctuations, T_{rms} and ρ_{rms}, show a lack of independence from SGS modeling and grid refinement in contrast to the velocity fluctuating field. The pressure fluctuations, which are assumed to be associated with the acoustic mode, are not significantly affected by the modeling and the mesh resolution. Furthermore, the comparison of different contributions to the viscous dissipation reveals that the solenoidal dissipation plays the most dominant role regardless of the model. Finally, it is found that the ILES is more likely to produce consistent results even though a small amount of numerical viscosity is introduced through a sixth-order skew-symmetric split-centered scheme to emulate the effects of unresolved scales.

Keywords: Subgrid-scale (SGS) modeling, Supersonic Turbulent Boundary Layer

*corresponding author: hadjadj@coria.fr

(STBL), Wall-adapting local eddy-viscosity (WALE), Dynamic Smagorinsky model (DSM), Coherent Structures model (CSM), Implicit LES (ILES)

1. Introduction

The study of supersonic turbulent boundary layers (STBL) is crucial for understanding basic flow physics in turbulent wall-bounded flows. The study has also a great importance in many industrial applications, such as high speed external and internal aerodynamics [1, 2, 3, 4], combustion and detonation [5, 6]. For adiabatic STBL, and due to viscous heating, compressibility effects arise mainly from the large change in the fluid properties (variable-density flow). It is then commonly concluded that adiabatic supersonic turbulent boundary layers at moderate Mach numbers (typically $M \leq 5$) can be studied using the same models as low-speed flows, as long as the variations in the mean flow properties are accounted for (see for example Morkovin 1961 [7], Bradshaw, 1977 [8] and Smits & Dussauge, 2006 [9]). Adiabatic supersonic turbulent boundary layers were first investigated through experiments, in order to validate the Morkovin's hypothesis (for a large data compilation, see Fernholz & Finley, 1977 [10]).

Three-dimensional numerical simulations of turbulent boundary layer are usu-ally classified as direct Navier-Stokes simulations (DNS) and large-eddy simulations (LES). In a DNS all relevant scales of motions are numerically resolved and therefore a detailed representation of a turbulent flow field can be obtained. In LES, only large energy-containing eddies are numerically resolved. This is accomplished by filtering-out the high–frequency component of the flow field and using the low-pass-filtered form of the Navier-Stokes equations to solve for the large-scale component only. The effects of the filtered-out small-scale fields on the resolved fields are accounted for through the so-called subgrid-scale (SGS) model. Many different LES approaches have been developed for the construction of SGS models; some of these are described in this paper, which addresses their applicability in the case of supersonic turbulent flow over a flat plate at a zero-pressure-gradient. Our focus here is on developing a methodology for assessing LES approaches on a representative flow, which is the obvious pre-requisite before applying these models to more complex geometries.

Among others, Spyropoulos & Braisdell (1998) [11] reported LES of spatially-evolving supersonic turbulent boundary layer at Mach number $M = 2.25$. Because of the low considered Mach number, the modeling of the isotropic part of the shear stresses was not found to have a considerable effect on the skin-friction coefficient, C_f. The insufficient amount of turbulent transport was attributed to the use of the dynamic Smagorinsky model, in which the eddy viscosity is computed using the smallest resolved scales. Hadjadj *et al.* (2015) [12] recently studied spatially-evolving STBL with cooled walls via well-resolved LES's. Also, supersonic flat-plate boundary layers have been investigated by Yan *et al.* (2002) [13] using monotonically integrated large-eddy simulation (MILES) approach. In this simulation, the numerical dissipation induced by the scheme substitutes the SGS eddy viscosity, mimicking from an energetic view-point the action of SGS terms on the flow dynamics. Their results indicate that the subgrid-scale effects can be adequately modeled using MILES without the need for the Smagorinsky model.

In LES, the accuracy of the resolved scales highly relies on the mesh size. Locally refined grids usually lead to more resolved turbulent energy but with costly CPU time and memory requirements. The strategy in LES is then to make the best compromise between accuracy and computational costs. Dissipation of a given SGS model may originate, in different proportions, either from the resolved velocity fluctuations or from the mean-averaged velocity gradients. In the recent work of Ben-Nasr *et al.* (2016) [14], we presented a detailed study of a spatially-evolving STBL over a flat plate at $M_\infty = 2$ and $\mathrm{Re}_\theta \approx 2600$. Different SGS models (namely the wall-adapting local eddy-viscosity (WALE) model, the Dynamic Smagorinsky model (DSM) and the Coherent Structures model (CSM)) as well as grid resolutions were used in order to compare the contribution of the SGS modeling on turbulence. The advantage and superiority of CSM and WALE in resolving high-speed compressible turbulent boundary layer over flat plate is clearly established in that study over computationally costly DSM. It is also interesting to mention the performance of Implicit LES (ILES) with respect to other models. In the present study, we extend the previous work for higher Re_θ, while using wider spanwise domain for various LES models. Much coarser grid resolutions have been employed to assess the effectiveness of the LES modeling compared to well-resolved LESs presented in Ben-Nasr *et al.,* (2016) [14]. We further highlight the interesting features of these LESs in light of the near wall interactions of the fluctuating quantities as a natural sequel of the previous work. After a brief description of the numerical methodology and the problem setup in section 2, we present the flow analysis in section 3. Turbulence statistics up to fourth-order moments are reported in order to assess more specifically the near-wall behavior of the SGS models. Finally, the conclusions are drawn in section 4.

2. Numerical methodology and SGS modeling

For sake of brevity, we restrict the description of the governing equations used for the present study. The details of the numerical methodology as well as the modeling aspect can be found in Ben-Nasr *et al.,* (2016) [14]. The convective fluxes are discretized using a sixth-order locally-conservative skew-symmetric split-centered formulation [15]. The viscous fluxes are discretized using a fourth-order compact central differences scheme. Time advancement is assessed by a standard explicit Runge-Kutta algorithm of third-order.

2.1. Modeling the SGS tensor

The SGS stress tensor, $\tau_{ij} = \rho(\widetilde{u_i u_j} - \widetilde{u}_i\ \widetilde{u}_j)$ is modeled via the definition of a SGS eddy viscosity, μ_{sgs}, as

$$\tau_{ij} - \frac{1}{3}\ \tau_{kk}\,\delta_{ij} = -2\ \mu_{sgs}(\widetilde{S}_{ij} - \frac{1}{3}\widetilde{S}_{kk}\,\delta_{ij}) \tag{1}$$

where $\widetilde{S}_{ij} = \frac{1}{2}(\partial\widetilde{u}_i/\partial x_j + \partial\widetilde{u}_j/\partial x_i)$ is the strain rate tensor of the resolved scales. The above SGS viscosity can be expressed as: $\mu_{sgs} = \rho\, C_s \Delta^2|\widetilde{S}|$, where $|\widetilde{S}| = \sqrt{2\widetilde{S}_{ij}\widetilde{S}_{ij}}$ is the second invariant of the strain rate tensor, and C_s is a dynamically-retrieved modeling constant. We use Yoshisawa [16] closure for the isotropic part of the SGS stress tensor, $\tau_{kk} = 2\rho\, C_I \Delta^2|\widetilde{S}|^2$. The model constant, C_I, is dynamically calculated for the DSM procedure, or set equal to 0.005 for the CSM (Moin *et al.* [17]). Unless stated, the isotropic part of the SGS stress tensor, τ_{kk}, is not modeled for CSM and WALE models.

Dynamic Smagorinsky model

In the Dynamic Smagorinsky procedure, the two model's constants, C_s and C_I, are dynamically extracted from the resolved flowfield quantities. A *test* filter, denoted as $\widehat{(.)}$, whose width is larger than the grid-filter width, is applied to the grid-filtered quantities. The model's constants are then calculated at the *test*-filter wavenumber, and are assumed to remain about the same within $[k_{test},\ k_c]$ wavenumbers range. Denoting $\widehat{\Delta}$ as the *test*-filter width and Δ is the grid-filter width, it is common to define $\widehat{\Delta}/\Delta = 2$. After dynamically retrieving C_s and C_I, and to avoid any numerical instability due to negative values, both constants are averaged in the homogeneous direction (z), and clipped within [0, 0.08] and [0, 0.02], respectively.

Coherent structures model

For the coherent structures model, C_s is dynamically calculated using a function of the velocity gradient tensors. This function is based on the assumption which states that, for a well-resolved DNS grid, the SGS dissipation is small at the center of a coherent fine-scale eddy, and that the energy transfer between resolved and subgrid scales is located around this coherent eddy (Kobayashi [18]; Kobayashi [19];

Onodera *et al.* [20]). The model's constant, C_s, is thus defined by: $C_s = C_{csm}|F_{cs}|^{3/2}$ with $F_{cs} = \widetilde{Q}/\widetilde{E}$, where C_{csm} is a model's parameter (by default equal to 1/30) and F_{cs} is the coherent structures function. $\widetilde{Q}$ and $\widetilde{E}$ are respectively the second invariant of the resolved velocity gradient and the magnitude of a resolved velocity gradient tensor, given by:

$$\widetilde{Q} = \frac{1}{2}\left(\widetilde{\mathcal{W}}_{ij}\widetilde{\mathcal{W}}_{ij} - \widetilde{\mathcal{S}}_{ij}\widetilde{\mathcal{S}}_{ij}\right) \qquad \widetilde{E} = \frac{1}{2}\left(\widetilde{\mathcal{W}}_{ij}\widetilde{\mathcal{W}}_{ij} + \widetilde{\mathcal{S}}_{ij}\widetilde{\mathcal{S}}_{ij}\right) \tag{2}$$

with $\widetilde{\mathcal{S}}_{ij}$ and $\widetilde{\mathcal{W}}_{ij}$ are the velocity-strain tensor and the vorticity tensor in a grid scale flowfield, respectively. It follows that:

$$\widetilde{Q} = -\frac{1}{2}\frac{\partial \widetilde{u}_j}{\partial x_i}\frac{\partial \widetilde{u}_i}{\partial x_j} \qquad \widetilde{E} = \frac{1}{2}\frac{\partial \widetilde{u}_j}{\partial x_i}\frac{\partial \widetilde{u}_j}{\partial x_i} \tag{3}$$

Note that $-1 \leq F_{cs} \leq 1$, which assume that the model's constant is bounded ($0 \leq C_s \leq 0.05$) and admits a weak variance.

Wall-Adapting Local Eddy-viscosity model

The WALE model estimates the eddy viscosity, based on the invariants of the velocity gradient as:

$$\mu_{sgs} = \bar{\rho}\Delta^2 C_w^2 \frac{\left(\widetilde{\mathcal{S}}^*_{ij}\widetilde{\mathcal{S}}^*_{ij}\right)^{3/2}}{\left(\widetilde{S}_{ij}\widetilde{S}_{ij}\right)^{5/2} + \left(\widetilde{\mathcal{S}}^*_{ij}\widetilde{\mathcal{S}}^*_{ij}\right)^{5/4}} \tag{4}$$

with

$$\widetilde{\mathcal{S}}^*_{ij} = \frac{1}{2}\left(\widetilde{g}^2_{ij} + \widetilde{g}^2_{ji}\right) - \frac{1}{3}\widetilde{g}^2_{kk}\delta_{ij} \qquad \widetilde{g}^2_{ij} = \widetilde{g}_{ik}\widetilde{g}_{kj} \tag{5}$$

C_w is a model's constant, by default taken equal to 0.5 (Nicoud & Ducros [21]) and $\widetilde{g}_{ij} = \partial\widetilde{u}_i/\partial x_j$.

2.2. Modeling the SGS heat flux

By analogy to the SGS stress tensor modeling, the SGS heat flux is modeled using an eddy-viscosity formulation, which can be written as:

$$\frac{1}{\gamma - 1}\frac{\partial\left(\overline{pu_j} - \overline{p}\widetilde{u}_j\right)}{\partial x_j} = -\frac{\mu_{sgs}}{Pr_{sgs}} C_p \frac{\partial \widetilde{T}}{\partial x_j} \tag{6}$$

The SGS Prandtl number, Pr_{sgs}, is taken constant and equal to 0.9.

2.3. Problem setup

The incoming boundary layer is spatially evolving at a freestream Mach number, $\mathrm{M}_\infty = 2$, and an inlet Reynolds number, $\mathrm{Re}_{\tau_{in}} = \rho_w u_\tau \delta_{in}/\mu_w \approx 450$ or $\mathrm{Re}_{\theta_{in}} = \rho_\infty u_\infty \theta_{in}/\mu_\infty \approx 2000$ (where u_τ is the friction velocity, δ_{in} is the inflow boundary layer thickness and θ_{in} is the momentum thickness at the inlet).

The computational domain used in this study is a box having a size of $L_x \times L_y \times L_z = 106\ \delta_{in} \times 9.13\ \delta_{in} \times 4.77\ \delta_{in}$ in the streamwise (x), wall-normal (y) and spanwise (z) directions, respectively.

As shown in table 1, different grid resolutions are used with uniformly spaced grid in both streamwise and spanwise directions. Clustered grid is used in the wall-normal direction based on a stretching function $L_y \sinh(\beta\eta)/\sinh(\beta)$, where L_y is the the box size in the y-direction and the β is the stretching factor. The mapped coordinate η is equally spaced and varies between 0 and 1. The flowfield is initialized using a digital filter procedure based on Klein's method (Klein *et al.*, 2004 [22]) where the *r.m.s.* velocity profiles are extracted from the DNS of Bernardini and Pirozzoli (2011) [23]. A series of approximately 140 characteristic times, $\tau_c = \delta_{in}/u_\infty$, is achieved to sweep the initial transient solution. Then, turbulence statistics are sampled and extracted each time step from time series covering $\tau \approx 300\tau_c$. By plotting the time evolution of the main boundary layer statistics, such as the boundary layer thickness and the friction velocity, this sampling time is judged to be sufficient to reach a statistical convergence of the considered quantities. A reference simulation (*e.g.* CSM-M90 case) is performed over about 40 hours using 64 processors, for a total of about 2560 CPU hours.

The First-half of the computational domain is dedicated to the recycling/rescaling procedure, while the second-half is used for data analysis. In the latter domain, Re_τ approximately ranges from 950 to 1250 and Re_θ from 4000 to 6000. Table 2 reports statistical properties of the considered test-cases at a given station $x_{res} \simeq 92.8\delta_{in}$, which corresponds to $\mathrm{Re}_\tau \approx 1100$.

3. Results and discussions

3.1. Basic flow organization

It is known that the inner part of the boundary layer is occupied by alternating streaks of high- and low-speed fluids. These streaks are presumed to derive from elongated, counter-rotating streamwise vortices near the wall. At $y^+ < 100$, those streaks are shown to significantly contribute to the turbulence production, which

Case	N_x	N_y	N_z	Δx^+	Δy^+_{min}	Δz^+	β
DNS [24]	7680	331	800	$6.84 - 6.57$	0.7	$5.91 - 5.67$	–
M45	768	45	96	$66 - 69$	~ 1.9	$24 - 25$	6.55
M90	768	90	96	$66 - 69$	~ 1.3	$24 - 25$	6.15
M180	768	180	96	$66 - 69$	~ 1.2	$24 - 25$	5.45

Table 1: Grid resolution sensitivity study using the CSM. Subscript (+) denotes the normalization by the friction velocity, with $y^+ = y\, u_\tau/\nu_w$.

Case	Re_τ	Re_θ	10^3 C_f	δ^*/δ	10^2 θ/δ	H	T_w/T_∞	M_τ	$\sqrt{\langle p'^2_w \rangle}/\tau_w$
DNS [24]	1113.4	6044.1	2.11	0.250	8.57	2.92	1.717	0.0649	–
DSM	1076.9	5866.4	1.86	0.288	9.64	2.98	1.56	0.0611	5.94
CSM	1216.6	5532.1	2.39	0.247	8.48	2.91	1.659	0.0691	4.58
WALE	1150.6	5236.4	2.33	0.237	8.61	2.75	1.621	0.0682	4.16
ILES	1050.2	5457.5	2.20	0.293	8.97	3.26	1.707	0.0767	4.81

Table 2: Boundary layer properties using M90 grid for different subgrid models. $\mathrm{Re}_\tau = \rho_w u_\tau \delta/\mu_w$; $\mathrm{Re}_\theta = \rho_\infty u_\infty \theta/\mu_\infty$; $\mathrm{C}_f = 2\tau_w/\rho_\infty u^2_\infty$; $H = \delta^*/\theta$; $\mathrm{M}_\tau = u_\tau/(\gamma \mathcal{R} T_w)^{1/2}$, δ^* is the displacement thickness.

Case	Line	Symbol
DNS		○
DSM	—	■
CSM	– –	▲
WALE	· · ·	◆
ILES	· — ·	▼
M45	—	▲
M90	—	■
M180	—	●

Table 3: Lines and symbols of the different cases.

Case	Re_τ	Re_θ	$10^3\ \mathrm{C}_f$	δ^*/δ	$10^2\ \theta/\delta$	H	T_w/T_∞	M_τ	$\sqrt{\langle p'^2_w \rangle}/\tau_w$
CSM-M45	1148.6	5207.8	2.35	0.249	8.40	2.96	1.653	0.0686	4.45
CSM-M90	1216.6	5532.1	2.39	0.247	8.48	2.91	1.659	0.0691	4.58
CSM-M180	1117.1	5586.6	2.35	0.278	9.25	3.00	1.657	0.0684	4.57

Table 4: Boundary layer properties for different grids using the CSM.

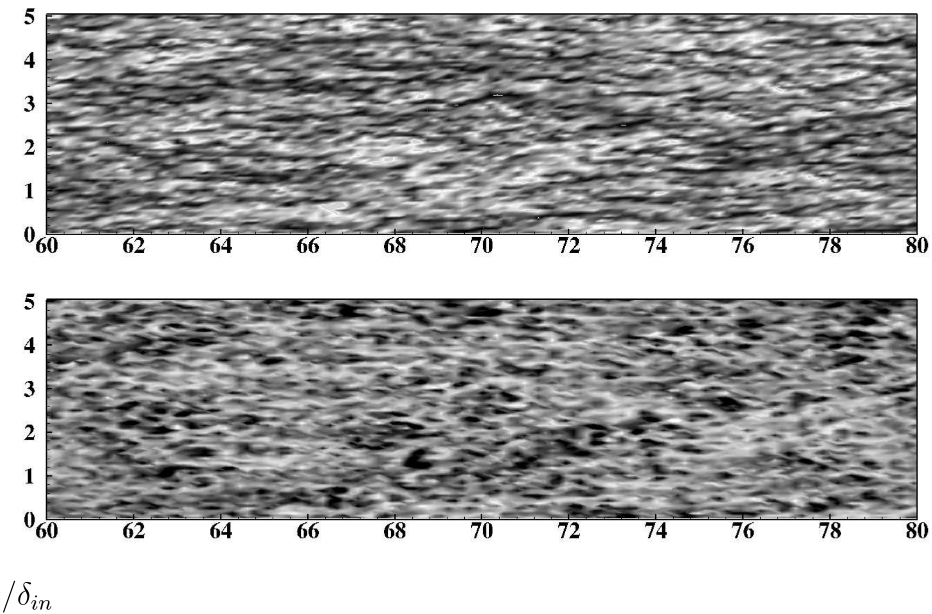

Figure 1: Instantaneous (a) velocity- and (b) temperature-fluctuation fields in the x-z plane at $y^+ \simeq 25$, for using the CSM-M90. Contour levels are shown for (a) $-0.25 \leq u'/u_\infty \leq 0.25$ and (b) $-0.25 \leq T'/T_\infty \leq 0.25$, from dark to light shades.

occurs during the *bursting* process: low-speed streaks would gradually lift up from the wall, oscillate, and then break up violently, ejecting fluid away from the wall and into the outer layer (Smits & Dussauge, 2006 [9]).

In order to qualitatively assess the turbulent nature of the flow in the log layer, wall-parallel slices of velocity and temperature fluctuations are plotted in Fig. 1 in a wall-parallel plane at $y^+ \simeq 25$. The data are obtained using the CSM-M90. As reported by Pirozzoli & Bernardini (2011) [24] and Duan *et al.* (2010) [25], Fig.(1-a) shows bearly alternating high- and low-speed streaks, which corresponds to positive and negative velocity fluctuations, respectively. For the temperature field, Fig. (1-b) shows similar structured patterns, with alternated dark and light shades. These can be interpreted as the anti-correlated character that links the velocity and temperature fluctuations close to solid walls.

Fig. (2) shows that the distributions of the auto-correlation functions (for the different meshes for CSM at different y^+) drop rapidly towards zero when L_z increases. Note that all other cases exhibits similar behavior and are not shown here. We can thus consider that the spanwise domain extent is wide enough to not inhibit turbulence dynamics in z-direction. This confirms the previous observation made on the streaks development in the x-z wall-parallel plane.

3.2. Thermodynamic properties and Strong Reynolds Analogy

Figs. (3-a; 3-c) show the wall-normal distribution of the normalized *r.m.s* of some thermodynamic quantities when varying SGS models and Figs. (3-b; 3-d; when varying the grid resolutions. Overall, the results show similar levels of these quantities when varying the SGS models. The *r.m.s* of temperature, T_{rms}, exhibits a peak near the wall ($y/\delta \simeq 0.015$) where it reaches a maximum of bit higher than T_∞ and decreases afterward to 2% of T_∞ outside the boundary layer. At the wall, the *r.m.s* of pressure, p_{rms}, reaches a maximum of 3% of p_∞ for the CSM & DSM, and decreases within the layer reaching 0.8% near the edge of the boundary layer. For the WALE mode, these properties remain lowest compared to the other models. For the ILES, a *bump* of T_{rms} is present in the outer region of the boundary layer $y/\delta > 0.2$, probably due to a lack of energy dissipation in this region. The *r.m.s* quantities show a monotone increase when coarsening the grid for temperature and density, while p_{rms} remains insensitive with grid refinement. The observed *bump* is found to be sensitive to the grid resolution for T_{rms} which can confirm an accumulation of non-dissipated energy in this region of the flow. For an adiabatic supersonic turbulent boundary layer, it is commonly known that u' and T' are supposed to be perfectly anti-correlated and that the *Strong Reynolds Analogy* relation, linking the *r.m.s* of the temperature and the velocity fluctuations, equals nearly 1.

By definition, the *r.m.s* of the temperature fluctuations is defined as:

$$\langle T'T' \rangle = \left(\frac{\gamma - 1}{\gamma \mathcal{R}} \right)^2 \langle u \rangle^2 \langle u'u' \rangle + 2\langle T'T'_t \rangle - \langle T'_t T'_t \rangle \tag{7}$$

where T'_t is the total temperature fluctuations. The angle brackets represent an ensemble average approximated by a volume and a time average. If it is assumed that the following condition holds (Guarini *et al.*, 2000 [26]; Pirozzoli *et al.*, 2004 [27]):

$$\frac{\langle T'T' \rangle}{\langle T \rangle^2} \gg \frac{\langle T'_t T'_t \rangle - 2\langle T'T'_t \rangle}{\langle T \rangle^2} \tag{8}$$

Eq. (7) then reads:

$$\langle T'T' \rangle^{1/2} \approx \frac{\gamma - 1}{\gamma \mathcal{R}} \langle u \rangle \langle u'u' \rangle^{1/2} \tag{9}$$

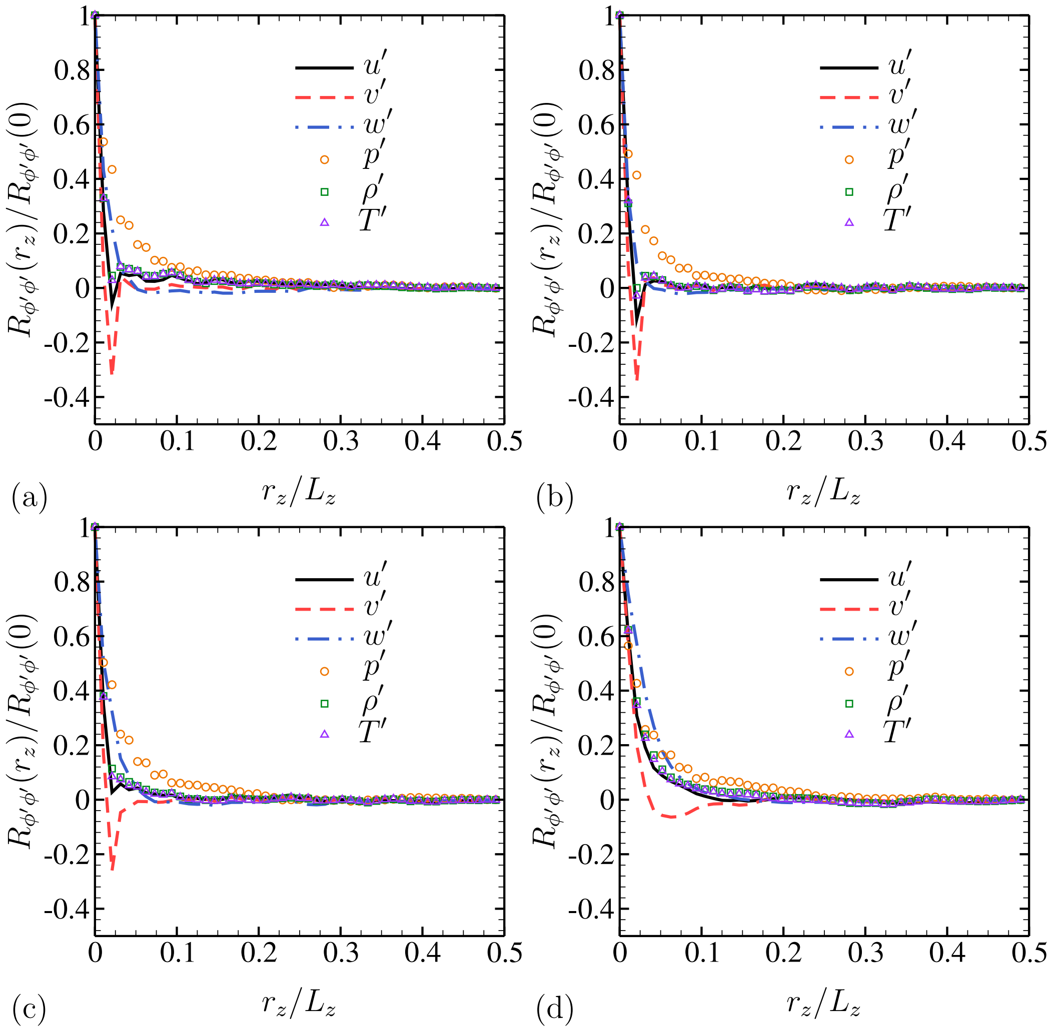

Figure 2: Instantaneous auto-correlation coefficients (a) at $y^+ \simeq 30$ for CSM-M45, (b) at $y^+ \simeq 10$ for CSM-M90, (c) at $y^+ \simeq 30$ for CSM-M90, (d) at $y^+ \simeq 100$ for CSM-M90.

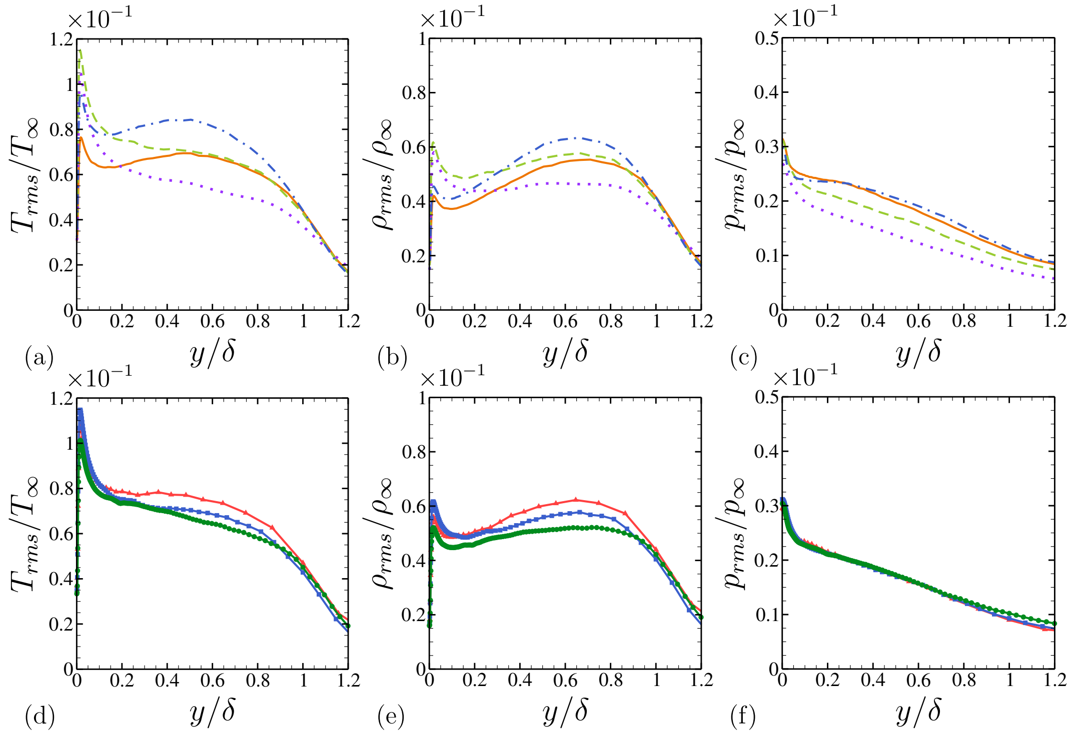

Figure 3: Normalized *r.m.s.* of the thermodynamic quantities as a function of y/δ. (a-b-c) Different SGS models using M90 grid; (d-e-f) Grid sensitivity study using CSM. See table 3 for legends.

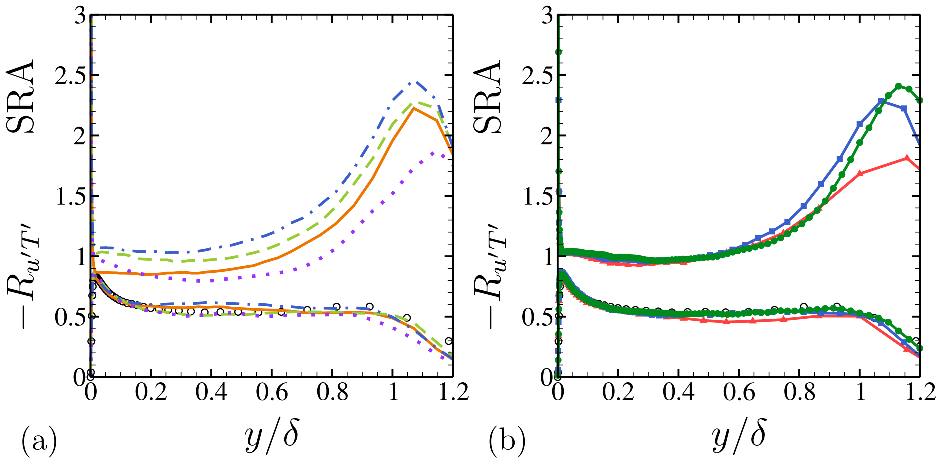

Figure 4: SRA and $-R_{u'T'}$ correlations as a function of y/δ. Circle: Pirozzoli et al. (2004) [27]. (a) Different SGS models using M90 grid; (b) Grid sensitivity study using CSM. For legends, see table 3.

and the $R_{u'T'}$ and $R_{u'v'}$ correlations are:

$$R_{u'T'} = -1 + \frac{\langle T'_t T'_t \rangle}{2\langle T'T' \rangle} \tag{10}$$

$$R_{u'v'} = -R_{v'T'}\left(1 - \frac{\langle v'T'_t \rangle}{\langle v'T' \rangle}\right) \tag{11}$$

Finally, if the total temperature is supposed to be uniform and the total temperature fluctuations are neglected, the SRA and the velocity-temperature correlation $R_{u'T'}$ become:

$$\begin{aligned} \text{SRA} &= \frac{\sqrt{\langle T'T' \rangle}/\langle T \rangle}{(\gamma - 1)\, M_\infty^2 \sqrt{\langle u'u' \rangle}/\langle u \rangle} \approx 1 \\ R_{u'T'} &= \frac{\langle u'T' \rangle}{\sqrt{\langle u'u' \rangle}\sqrt{\langle T'T' \rangle}} \approx -1 \end{aligned} \tag{12}$$

The SRA is found to hold very near to unity $0.8 - 1.2$ for about 70% (Fig. 4) of the boundary layer for all models as well as for the ILES. However, the CSM estimates a value of SRA ≈ 1 in almost 60% of the boundary layer. The SRA is also found to weakly be grid dependent. The deviations become larger for coarser mesh M45 near the edge of the boundary layer.

Previous studies predicted lower values of $-R_{u'T'}$, ranging between ≈ 0.55 and 0.8 (Pirozzoli *et al.*, 2004 [27]; Duan *et al.*, 2010 [25]; Pirozzoli & Bernardini, 2011 [24]). In the present simulations, $-R_{u'T'}$ lies between 0.5 and 0.6 for $0.2 < y/\delta < 0.8$, and rises to 0.8 at $y/\delta \simeq 0.02$. All models predict almost the same range of value. The velocity-temperature correlation, $-R_{u'T'}$, is found to be slightly sensitive to the grid resolution, decreasing when coarsening the grid (Fig. 4). At the vicinity of the boundary layer, $-R_{u'T'}$ drops gradually matching the previous DNS studies. This weak u' and T' anti-correlation can be attributed to the non-negligible total-temperature fluctuations within the boundary layer.

Considering a polytropic behavior of the thermodynamic quantities (Lechner *et al.*, 2001) [28], the correlation between the density and the temperature fluctuations is:

$$R_{\rho'T'} = \frac{\langle \rho' T' \rangle}{\sqrt{\langle \rho'\rho' \rangle}\sqrt{\langle T'T' \rangle}} \approx \frac{\sqrt{\langle \rho'\rho' \rangle}}{\sqrt{\langle T'T' \rangle}} \frac{\langle T \rangle}{\langle \rho \rangle} = -1 \tag{13}$$

In a wide region of the boundary layer (see Fig. 5), ρ' and T' are anti-correlated, and $-R_{\rho'T'}$ remains very close to unity. The correlation $-R_{\rho'T'}$ is also found to be insensitive to the SGS models as well as to the grid resolutions. The $-R_{u'v'}$ correlation's behavior (Fig. 5) is also confident with theoretical observations: constant in the region $0.1 \leq y/\delta \leq 0.8$ and then decrease beyond this region (Spina *et al.*, 1994) [29]. At $0.2 < y/\delta < 0.8$, all models show the same trends regardless of the grids ($0.41 < -R_{u'v'} < 0.49$). Both $-R_{u'v'}$ and $R_{v'T'}$ are found to be fairly correlated, and nearly equal to ≈ 0.5 in the outer-region of the boundary layer ($0.2 < y/\delta < 0.8$). These results are also in good agreement with the experimental data of Klebanoff [30] ($-R_{u'v'} \approx 0.5$). The effect of the SGS models on $R_{u'v'}$ and $R_{v'T'}$ in this region is weak. However for coarse mesh M45, both correlations show lower prediction throughout the wall-normal direction.

The resolved turbulent Prandtl number, Pr_t, is defined as:

$$\begin{aligned} Pr_t &= \frac{\langle \rho u'v' \rangle \partial \langle T \rangle / \partial y}{\langle \rho v'T' \rangle \partial \langle u \rangle / \partial y} \\ &= \left(1 - \frac{\langle \rho v' T_t' \rangle}{\langle \rho v'T' \rangle}\right)\left(1 - \frac{\partial \langle T_t \rangle}{\partial \langle T \rangle}\right)^{-1} \end{aligned} \tag{14}$$

Assuming a uniform total temperature in Eq. (14) yields to $\mathrm{Pr}_t = 1$. Fig. (6) shows that this assumption is not satisfied in a wide region of the boundary layer $y/\delta > 0.2$, $\mathrm{Pr}_t < 0.8$. This tendency is sensitive to grid coarsening near the

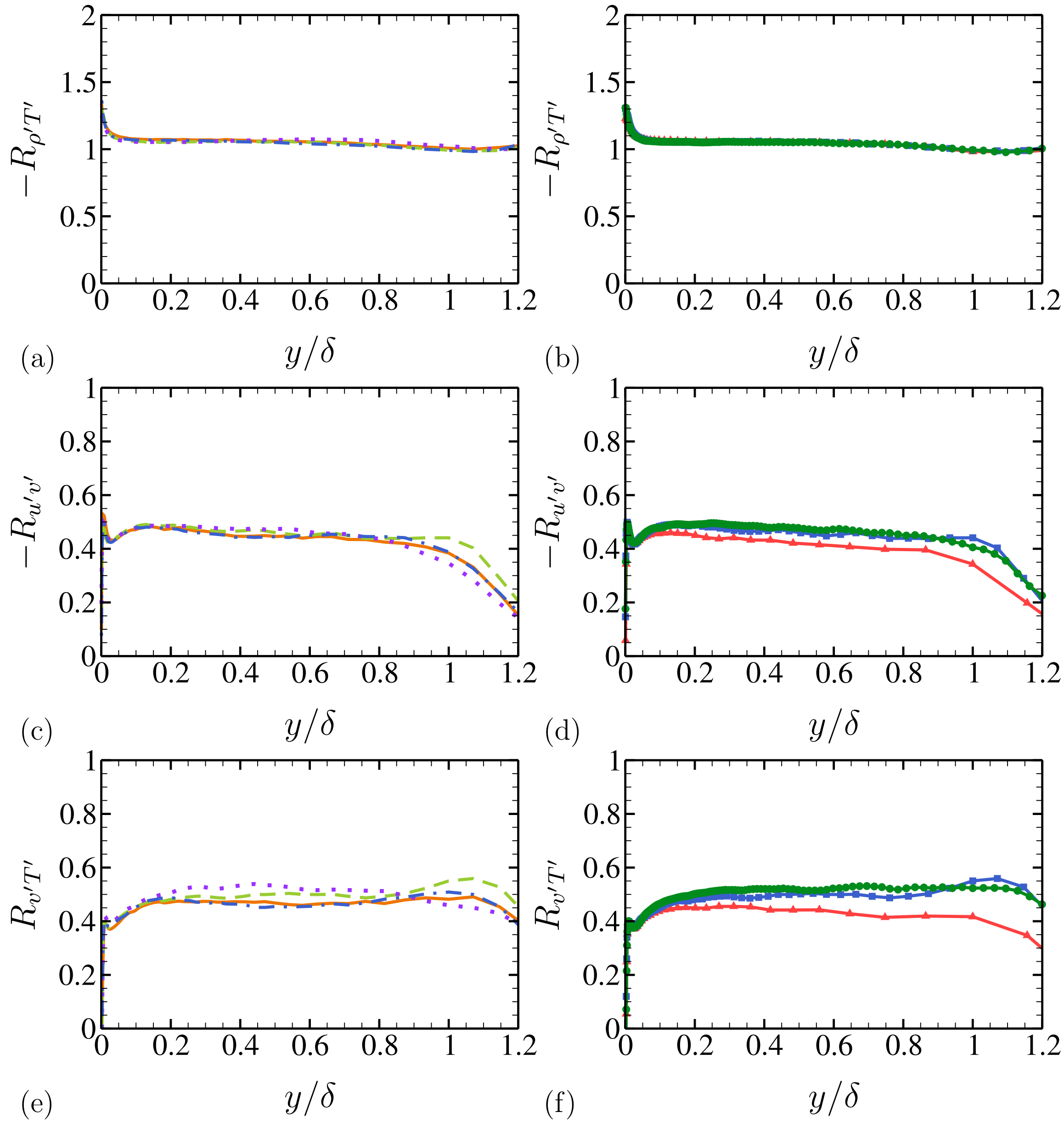

Figure 5: $-R_{\rho'T'}$, $-R_{u'v'}$ and $R_{v'T'}$ correlations as a function of y/δ. (a-c-e) Different SGS models using M90 grid; (b-d-f) Grid sensitivity study using CSM. For legends, see table 3.

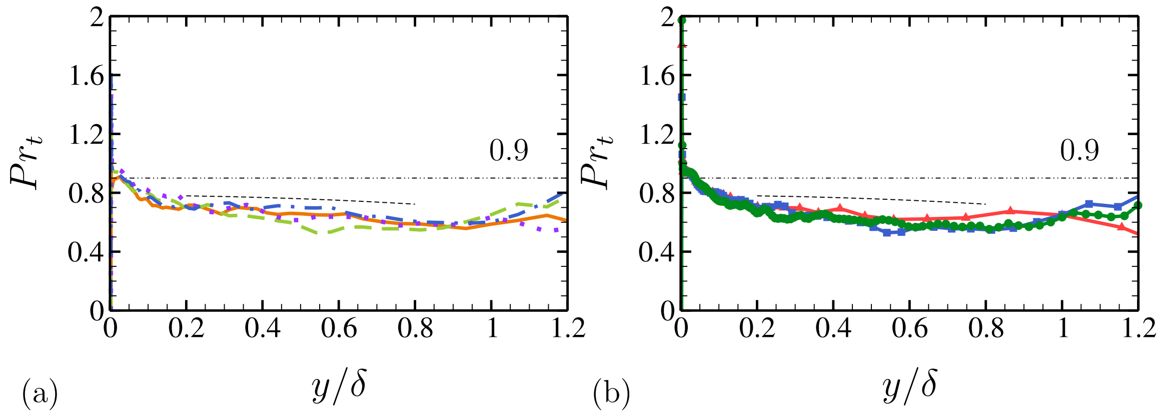

Figure 6: Resolved turbulent Prandtl number as a function of y/δ. (−−) DNS curve-fitting in Eq. (15). (a) Different SGS models using M90 grid; (b) Grid sensitivity study using CSM. For legends, see table 3.

outer region of the boundary layer. Pirozzoli *et al.* (2004) [27] proposed a curve-fitting of their supersonic boundary layer DNS data at $\mathrm{Re}_{\delta_2} \approx 2400$ in the region $0.2 < y/\delta < 0.8$:

$$Pr_t \approx 0.783 - 0.094 \left(\frac{y}{\delta}\right)^2 \tag{15}$$

It is found that the present results slightly under-estimate this curve-fitting.

3.3. Turbulence behavior

3.3.1. Anisotropy invariants map

The behavior of turbulent wall-bounded flows can be analyzed by examining the evolution of the anisotropy through the turbulent stresses, $\langle u_i' u_j' \rangle$, which can be qualified using the anisotropy tensor, defined as $a_{ij} = \langle u_i' u_j' \rangle - \frac{2}{3} K \delta_{ij}$, where δ_{ij} is the Kronecker tensor and $K = \frac{1}{2}\langle u_i' u_i' \rangle$ is the turbulent kinetic energy. The normalized anisotropy tensor, $b_{ij} = \frac{1}{2} a_{ij}/K$, is then simply defined as:

$$b_{ij} = \frac{1}{2}\frac{\langle u_i' u_j' \rangle}{K} - \frac{1}{3}\delta_{ij} \tag{16}$$

The anisotropy tensor has three invariants, the first being simply the trace of the tensor and is zero by definition. Therefore, any turbulent state can be fully

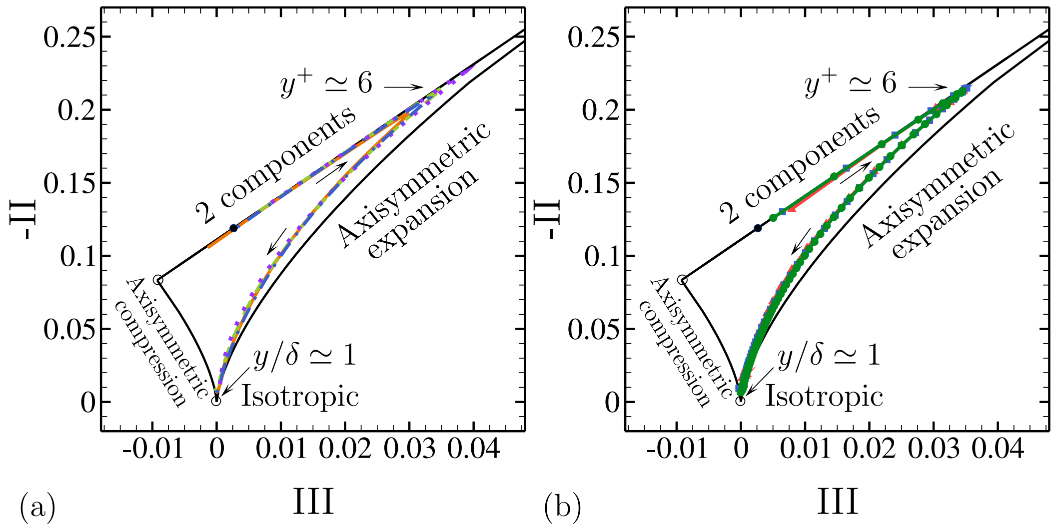

Figure 7: Anisotropy invariants maps. (a) Different SGS models using M90 grid; (b) Grid sensitivity study using CSM. For legends, see table 3.

characterized by the second and the third invariants, given by:

$$\mathrm{II} = b_{ij}b_{ji} = \frac{1}{2}b_{ii}^2, \qquad \mathrm{III} = b_{ij}b_{jk}b_{ki} = \frac{1}{3}b_{ii}^3 \tag{17}$$

According to Lumley (1978) [31], any realizable quantity associated with the fluctuating field must fall within the anisotropy map or on its boundaries. An analysis of the variation of these points and curves in the anisotropy invariants map can help highlighting the change of turbulence state. As can be seen in Fig. (7), the computed anisotropy maps for different models and grids lie inside the theoretical map, showing basically the same trends. Very close to the wall, the wall-normal fluctuation component, $\langle v'^2 \rangle$, quickly vanishes compared to the other two components, $\langle u'^2 \rangle$ and $\langle w'^2 \rangle$, making the turbulence state approximately two-dimensional. Here, the two–dimensionality means a two-component flow because $\langle u'^2 \rangle$ and $\langle w'^2 \rangle$ vary in the y-direction (Pope, 2000) [32]. Moving progressively inside the boundary layer, a state of an axisymmetric expansion is observed up to the outer edge of the boundary layer ($y \simeq \delta$), where the turbulence state is near-isotropic, and thus located near the origin of the map. This behavior of the turbulence is well reproduced by the current simulations in accordance with previous studies (Krogstad & Torbergsen, 2000 [33]; Shahab *et al.*, 2011 [34]).

3.3.2. Skewness and flatness factors

Higher-order moments such as the skewness and the flatness factors of the velocity fluctuations can be calculated for better analysis of the turbulence nature from statistics view-point. By definition, the skewness and flatness coefficients of a given velocity fluctuation are such as:

$$S(u_i') = \frac{\langle u_i'^3 \rangle}{\langle u_i'^2 \rangle^{3/2}}, \qquad F(u_i') = \frac{\langle u_i'^4 \rangle}{\langle u_i'^2 \rangle^{2}} \tag{18}$$

Their distribution along the boundary layer are plotted in Fig. (8) for different LES models and grid resolutions. Apart from the near-wall deviation of the skewness and flatness coefficients, the turbulence behavior is found to be nearly Gaussian, with $S(u') \approx 0$ (marginally negative) and $F(u') \approx 3$. This result is in good agreement with the DNS data. The peak position of both factors is correctly recovered by the LES, whereas their magnitudes are slightly over-estimated. For instance, $S(u')$ reaches a maximum within the range of $1.3 - 1.56$ against a maximum of 1 for the DNS. For $40 < y^+$, all agree well with the DNS database of Pirozzoli & Bernardini [24]. On the other hand, $F\,(u')$ maxima lies $\lesssim 6.6$ against a maximum of 5.15 for DNS. Nevertheless for $y^+ \geq 10$, all SGS models agree well with the DNS data. Both skewness and flatness are found to be less sensitive to the grid refinement. Among the models, the DSM shows largest deviation from the DNS data.

3.3.3. Near-wall asymptotic behavior

By means of the continuity equation and the non-slip wall boundary conditions, Tamano (2002) [35] and Morinishi *et al.* (2004) [36] proposed a comparison of adiabatic and isothermal near-wall asymptotic behaviors for compressible and incompressible turbulent channel flows, expressed as a power of y^+. In the following, we examine the near-adiabatic-wall asymptotic behaviors of different turbulent quantities, such as the velocity fluctuations, the turbulent kinetic energy, the viscous dissipation and the fluctuations of thermodynamic quantities.

The turbulent fluctuations ϕ' of a given quantity ϕ can be expanded in terms of Taylor series of y^+ as follows:

$$\phi' = \xi_{1,\phi}(x,z,t) + \xi_{2,\phi}(x,z,t)\, y^+ + \xi_{3,\phi}(x,z,t)\, y^{+2} + \mathcal{O}(y^{+3}) \tag{19}$$

It is evident that, no-slip condition at the wall implies ξ_1 for all velocity fluctuating components are zero. For incompressible flow, satisfying the continuity equation at the wall additionally yields $\xi_2 = 0$ for v' as $\partial v'/\partial y\mid_w = 0$ and thus $v_{rms} \propto y^{+2}$. On the other hand, $u_{rms} \propto y^+$ and $w_{rms} \propto y^+$. It follows that $K^+ \propto y^{+2}$ and $\langle u'v' \rangle \propto y^{+3}$.

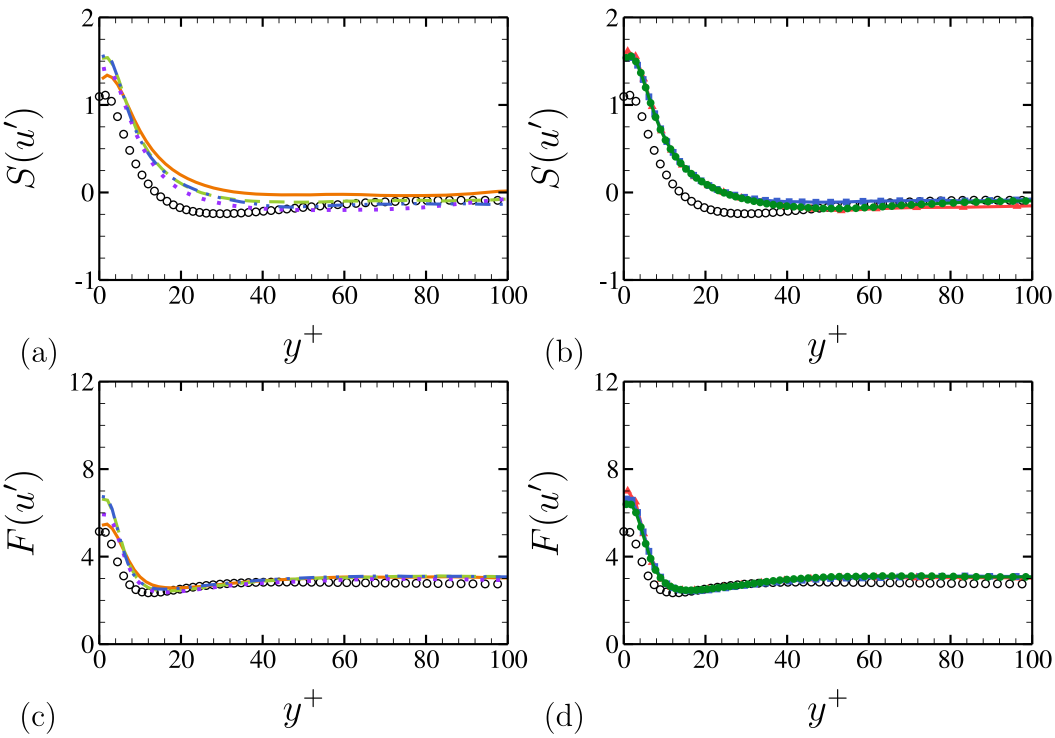

Figure 8: (a-b) Skewness and (c-d) Flatness factors as a function of y^+. For legends, see table 3.

Case	u^+_{rms}	v^+_{rms}	w^+_{rms}	$-\langle u'v'\rangle^+$	K^+	ε^+	$-\langle v'T'\rangle$	T_{rms}	ρ_{rms}	P_{rms}
Compressible	1	1	1	2	2	0	1	0	0	0
Incompressible	1	2	1	3	2	0	2	0	–	0

Table 5: Power indecies n of near-adiabatic-wall asymptotic behaviors.

The temperature and pressure distributions have a non-zero value at the wall, which implies that $T_{rms} \propto y^{+0}$ and $p_{rms} \propto y^{+0}$. This yields $\langle v'T'\rangle \propto y^{+2}$.

For a compressible turbulent flow, the main difference comes from the density variation with $\partial\rho/\partial t\mid_w \neq 0$ and ρ_{rms} presents a non-zero value asymptotic behavior, which yields $\partial u_i/\partial x_i\mid_w \neq 0$. According to Eq. (19), for a compressible u_{rms}, v_{rms} and w_{rms} present asymptotes $\propto y^+$. It follows that $K^+ \propto y^{+2}$, $\langle u'v'\rangle \propto y^{+2}$, and subsequently $\langle v'T'\rangle \propto y^+$.

The different power indices n ($\propto {y^+}^n$) of near-adiabatic-wall asymptotic behavior of different quantities are summarized in table 5.

Figs. (9-15) depict the near-wall asymptotic behaviors of the velocity fluctuations u^+_{rms}, v^+_{rms}, w^+_{rms} according to the Morkovin's scaling, as well as the Reynolds shear stress $\langle u'v'\rangle^+$, the normalized kinetic energy $K^+ = K/u_\tau^2$, the turbulent heat flux $-\langle v'T'\rangle$, the temperature fluctuations T_{rms} and the density fluctuations ρ_{rms} as a function of y^+ in *log-log* coordinates.

Figs. (9) and (11) show that, at the wall and up to the frontier of the viscous sublayer, u^+_{rms} and w^+_{rms} vary linearly with decreasing y^+. All SGS models exhibit excellent matching behavior for the different quantities, and all grid-resolution cases almost fairly compare with the near-wall required asymptotes, except at the wall region ($\Delta y^+_{min} \approx 1$), for coarsest mesh M45 $\Delta y^+_{min} \gtrsim 1.9$.

The difference in indices between the compressible and incompressible flows was mainly observed for v^+_{rms}, $-\langle u'v'\rangle^+$ and $-\langle v'T'\rangle$. Those asymptotes are plotted in Fig. (10;12;14), and show that, up to the considered wall-region ($\Delta y^+ \gtrsim 1$), the near-wall asymptotic behavior of v^+_{rms}, $-\langle u'v'\rangle^+$ and $\langle v'T'\rangle^+ = R_{v'T'}$ are better estimated using the incompressible indices ($\propto {y^+}^2$, ${y^+}^3$ and ${y^+}^2$, respectively), even if the Morkovin's scaling is not used for the Reynolds shear stress. In fact, according to Tamano (2002) [35], the theoretical compressible asymptotes of these quantities hold for the very near-wall region, *i.e.* at $y^+ \leq 1$. In the present simulations, M90 and M180 show quite good agreement for these quantities except v^+_{rms}, where very near to the

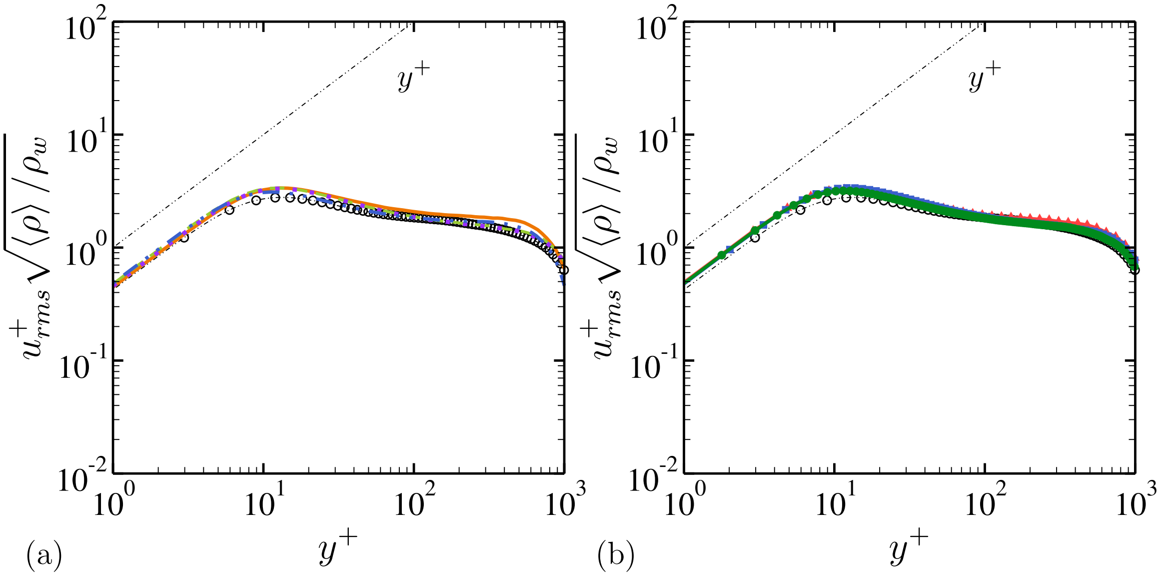

Figure 9: Near-wall asymptotic behavior of the streamwise velocity fluctuations u_{rms} in Morkovin's scaling as a function of y^+. (a) SGS models study using M90 grid; (b) Grid sensitivity study using CSM. For legends, see table 3.

wall the slope reduces as $\Delta y^+_{min} \gtrsim 1$.

Turbulent kinetic energy, K^+, varies linearly with decreasing ${y^+}^2$, while the viscous dissipation ε exhibits a non-zero constant behavior near the wall (Fig. 13). This tendency was also confirmed by Morinishi *et al.* (2004) [36], and this behavior is found to be unaffected mostly by varying the SGS model or the grid resolution. Morinishi *et al.* (2004) [36] also reported that the near-adiabatic-wall behavior of the thermodynamic quantities T_{rms}, ρ_{rms} and p_{rms} for a compressible flow, have a constant non-zero value asymptote $({y^+}^0)$ with decreasing y^+. As shown in Fig. (15), T_{rms}/T_∞, ρ_{rms}/ρ_∞ and p_{rms}/p_∞ exhibit an asymptote $\propto {y^+}^0$ when decreasing y^+. However, for a compressible flow near an isothermal wall, T_{rms} should vary linearly with decreasing y^+, while ρ_{rms} and p_{rms} do conserve a constant non-zero value asymptote with the same boundary condition.

Hence, for a near-adiabatic-wall region ($1 \leq y^+ \leq 6$), all statistics showed very good asymptotic behavior when compared to their incompressible flow counterparts discussed by Morinishi *et al.* (2004) [36]. The correlations $\langle u'v'\rangle^+$ and $\langle v'T'\rangle^+$ also showed acceptable behaviors compared to incompressible asymptotes although the mean-density variation is not taken into account.

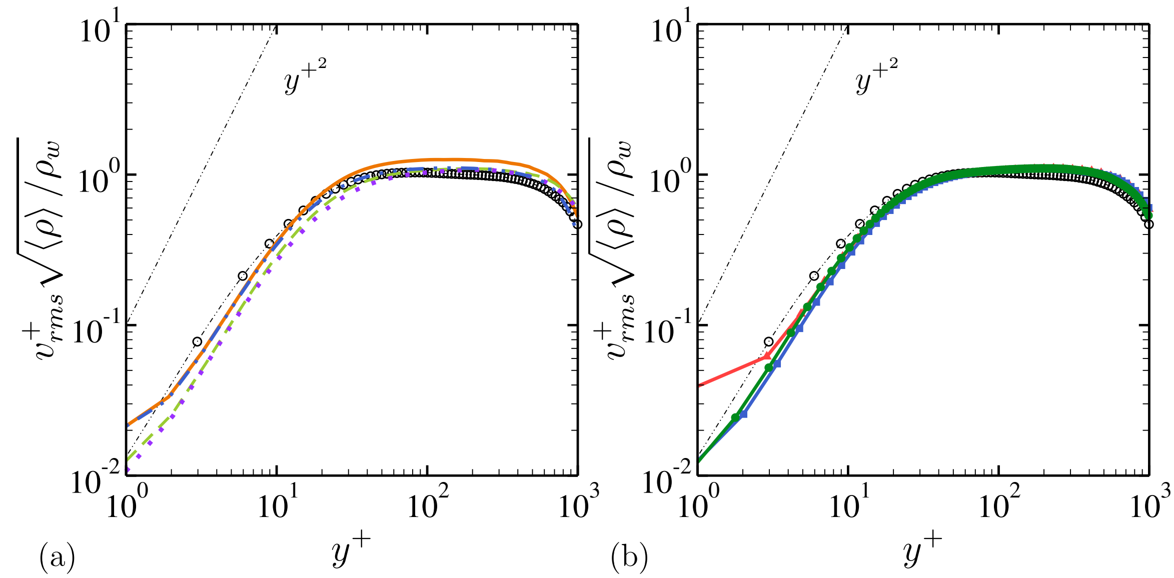

Figure 10: Near-wall asymptotic behavior of the wall-normal velocity fluctuations v_{rms} in Morkovin's scaling as a function of y^+. (a) Different SGS models using M90 grid; (b) Grid sensitivity study using CSM. For legends, see table 3.

3.4. Turbulent energy dissipation rate

In homogeneous compressible turbulence with constant viscosity, the turbulent energy dissipation is commonly written as the sum of two components, namely the solenoidal dissipation, ε_s, and the dilatational dissipation, ε_d. Additionally, in inhomogeneous turbulent flows, an inhomogeneous component of the dissipation, ε_I, is also present. Starting from the definition of the turbulent energy dissipation ε:

$$\overline{\rho}\varepsilon \equiv \left\langle \tau'_{ik}\frac{\partial u'_i}{\partial x_k} \right\rangle \tag{20}$$

where τ'_{ik} is [37]:

$$\begin{aligned} \tau'_{ik} \;=\; & \left[\mu'\left(\frac{\partial u'_i}{\partial x_k}+\frac{\partial u'_k}{\partial x_i}\right)-\frac{2}{3}\mu'\frac{\partial u'_l}{\partial x_l}\delta_{ik}\right]-\left[\left\langle \mu'\left(\frac{\partial u'_i}{\partial x_k}+\frac{\partial u'_k}{\partial x_i}\right)\right\rangle-\frac{2}{3}\left\langle \mu'\frac{\partial u'_l}{\partial x_l}\right\rangle\delta_{ik}\right] \\ + \; & \left[\mu'\left(\frac{\partial\langle u_i\rangle}{\partial x_k}+\frac{\partial\langle u_k\rangle}{\partial x_i}\right)-\frac{2}{3}\mu'\frac{\partial\langle u_l\rangle}{\partial x_l}\delta_{ik}\right]+\left[\langle\mu\rangle\left(\frac{\partial u'_i}{\partial x_k}+\frac{\partial u'_k}{\partial x_i}\right)-\frac{2}{3}\langle\mu\rangle\frac{\partial u'_l}{\partial x_l}\delta_{ik}\right] \end{aligned} \tag{21}$$

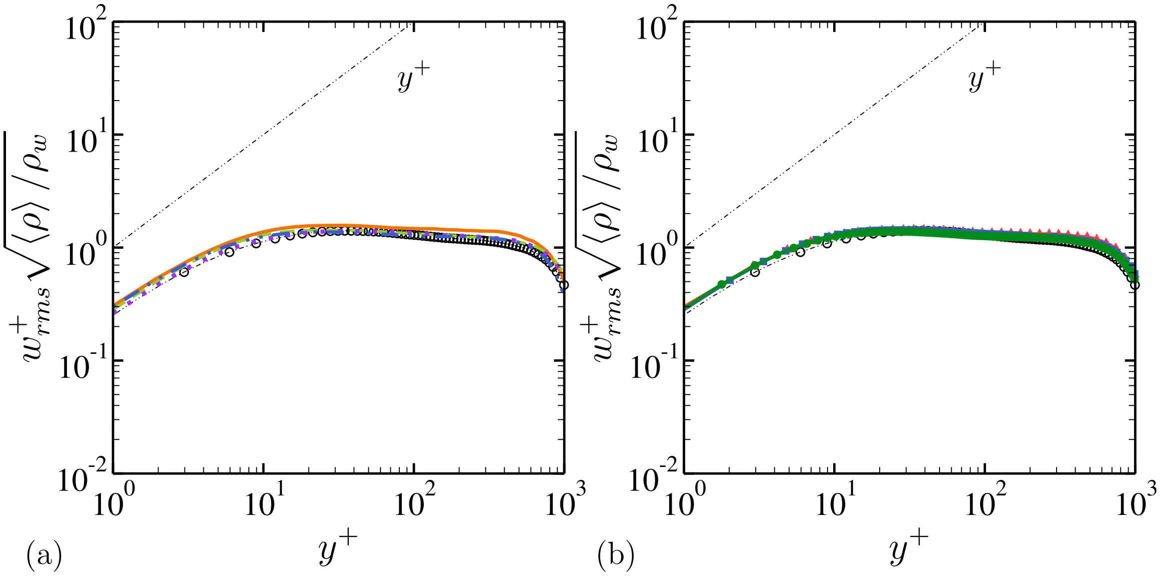

Figure 11: Near-wall asymptotic behavior of the spanwise velocity fluctuations w_{rms} in Morkovin's scaling as a function of y^+. (a) Different SGS models using M90 grid; (b) Grid sensitivity study using CSM. For legends, see table 3.

The total energy dissipation can be cast as the sum of three main parts $\varepsilon = \varepsilon_1+\varepsilon_2+\varepsilon_3$, where:

$$
\begin{aligned}
\overline{\rho}\varepsilon_1 &= \langle\mu\rangle \left\langle \frac{\partial u_i'}{\partial x_k}\left(\frac{\partial u_i'}{\partial x_k}+\frac{\partial u_k'}{\partial x_i}\right)\right\rangle - \frac{2}{3}\langle\mu\rangle \left\langle \frac{\partial u_i'}{\partial x_k}\frac{\partial u_l'}{\partial x_l}\right\rangle \delta_{ik} \\
\overline{\rho}\varepsilon_2 &= \left\langle \mu' \frac{\partial u_i'}{\partial x_k}\left(\frac{\partial u_i'}{\partial x_k}+\frac{\partial u_k'}{\partial x_i}\right)\right\rangle - \frac{2}{3}\left\langle \mu' \frac{\partial u_i'}{\partial x_k}\frac{\partial u_l'}{\partial x_l}\right\rangle \delta_{ik} \\
\overline{\rho}\varepsilon_3 &= \left\langle \mu' \frac{\partial\langle u_i\rangle}{\partial x_k}\right\rangle \left(\frac{\partial\langle u_i\rangle}{\partial x_k}+\frac{\partial\langle u_k\rangle}{\partial x_i}\right) - \frac{2}{3}\left\langle \mu' \frac{\partial u_i'}{\partial x_k}\right\rangle \frac{\partial\langle u\rangle_l}{\partial x_l}
\end{aligned}
\tag{22}
$$

The quantity $\varepsilon_1 = \varepsilon_s + \varepsilon_d + \varepsilon_I$ is also expressed as the sum of three contributions, namely, the solenoidal dissipation, ε_s, the dilatational dissipation, ε_d, and the inho-

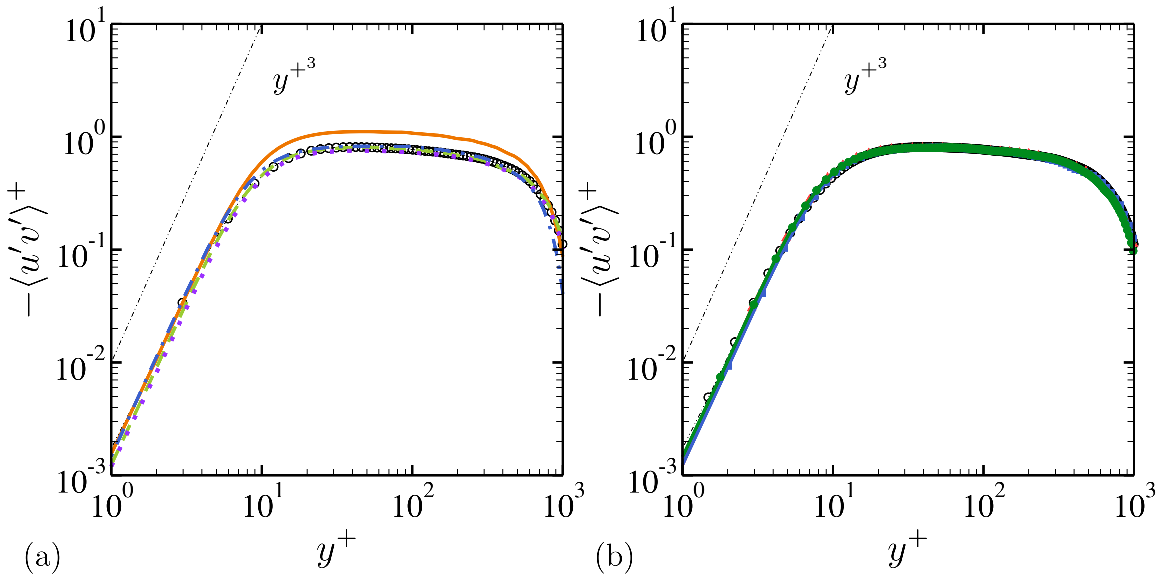

Figure 12: Near-wall asymptotic behavior of the normalized Reynolds shear stress $\langle u'v'\rangle^+$ as a function of y^+. (a) Different SGS models using M90 grid; (b) Grid sensitivity study using CSM. For legends, see table 3.

mogeneous dissipation, ε_I, given by:

$$\begin{aligned}
\overline{\rho}\varepsilon_s &= 2\langle\mu\rangle\langle\omega'_{ij}\omega'_{ij}\rangle \\
\overline{\rho}\varepsilon_d &= \frac{4}{3}\langle\mu\rangle\left\langle\frac{\partial u'_l}{\partial x_l}\frac{\partial u'_k}{\partial x_k}\right\rangle \\
\overline{\rho}\varepsilon_I &= 2\langle\mu\rangle\left(\frac{\partial^2\langle u'_i u'_j\rangle}{\partial x_i \partial x_j} - 2\frac{\partial}{\partial x_i}\left\langle u'_i\frac{\partial u'_j}{\partial x_j}\right\rangle\right)
\end{aligned} \quad (23)$$

Note that in our case, ε_s is directly deduced from $\varepsilon_s = \varepsilon_1 - \varepsilon_d - \varepsilon_I$. The turbulent energy dissipation rate is studied only using the CSM and the M90 grid. Fig. (16-a) shows the ratios of $\varepsilon_1/\varepsilon$, $\varepsilon_2/\varepsilon$ and $\varepsilon_3/\varepsilon$ as a function of y/δ for CSM-M90. It can be seen that ε_1 dominates the other components and that the contribution of μ' is negligible for such a flow. This is found to be true for all other LES models. Fig. (16-b) shows the ratios $\varepsilon_s/\varepsilon$, $\varepsilon_d/\varepsilon$ and $\varepsilon_I/\varepsilon$ as a function of y/δ, and shows that the solenoidal part of the dissipation is the most significant part. This result is true for all LES models. Contributions of ε_d and ε_I are found to be of the same order of magnitude.

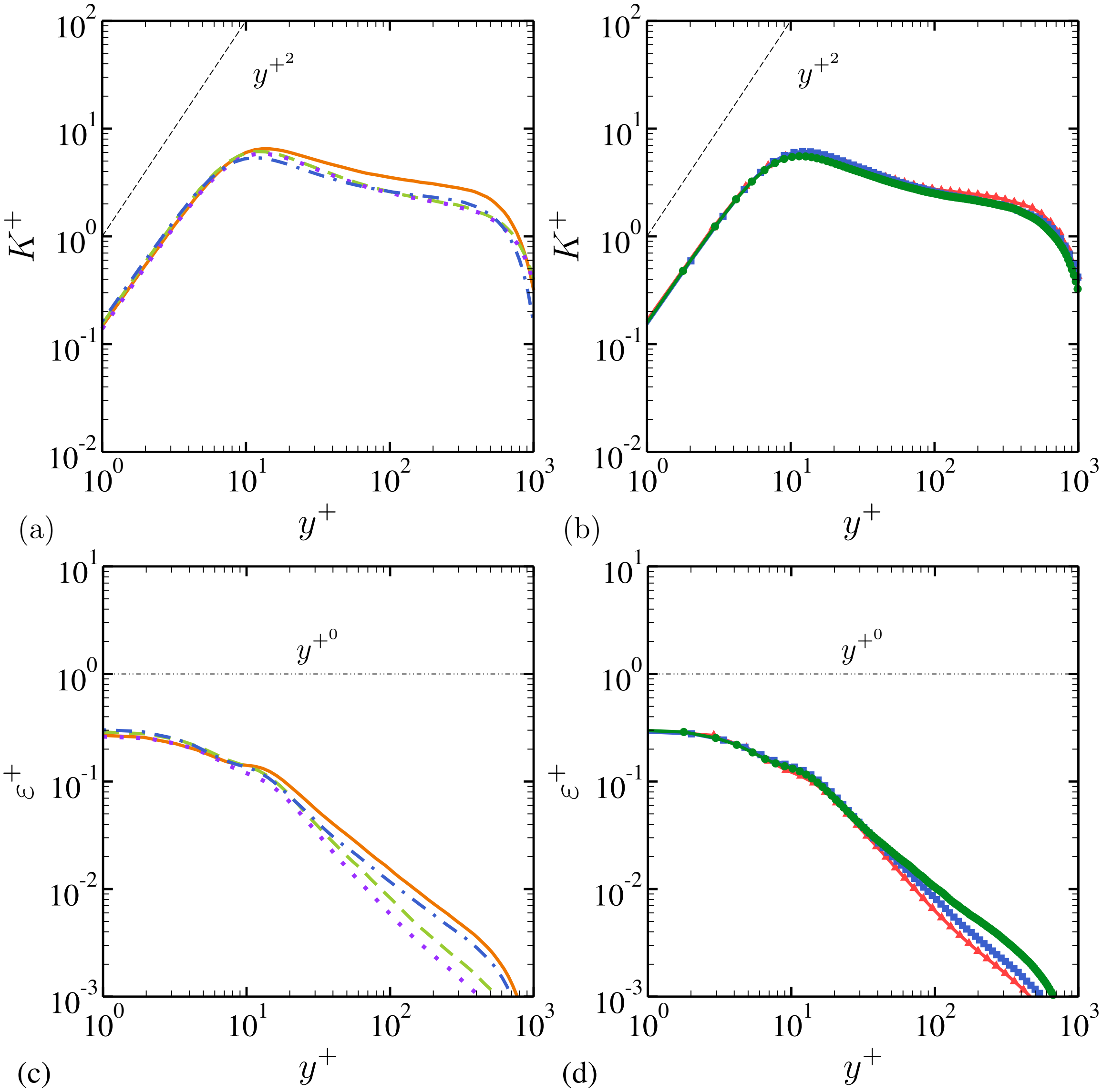

Figure 13: Near-wall asymptotic behavior of (a-b) dimensionless kinetic energy and (c-d) dimensionless molecular dissipation, $\varepsilon^+ = \varepsilon.\nu_w/(\rho_w u_\tau^4)$ as a function of y^+. For legends, see table 3.

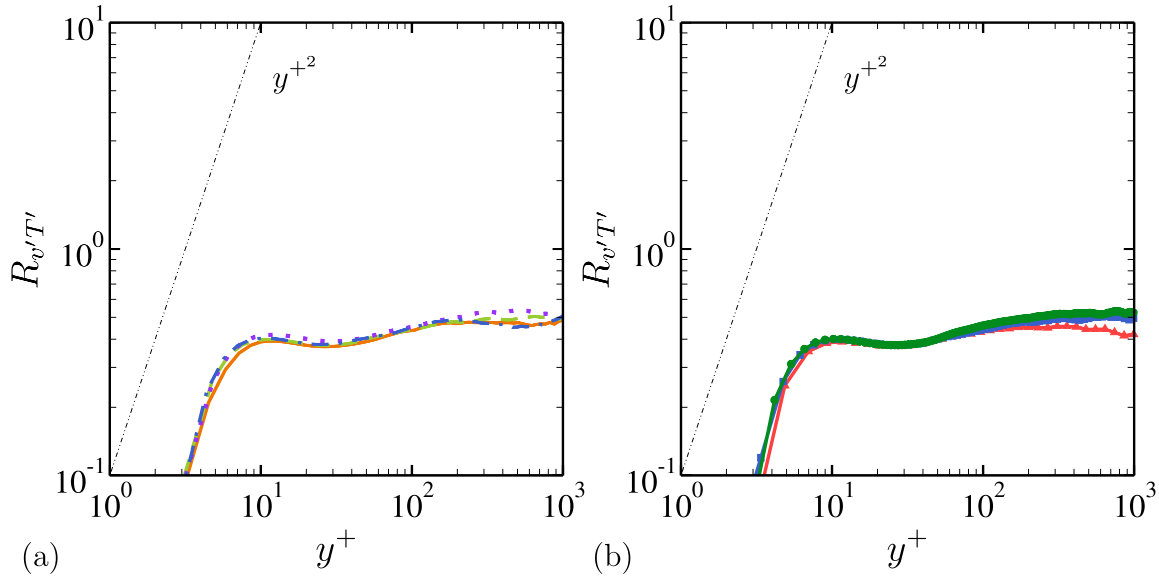

Figure 14: Near-wall asymptotic behavior of the normalized turbulent heat flux $R_{v'T'}$ as a function of y^+. (a) Different SGS models using M90 grid; (b) Grid sensitivity study using CSM. For legends, see table 3.

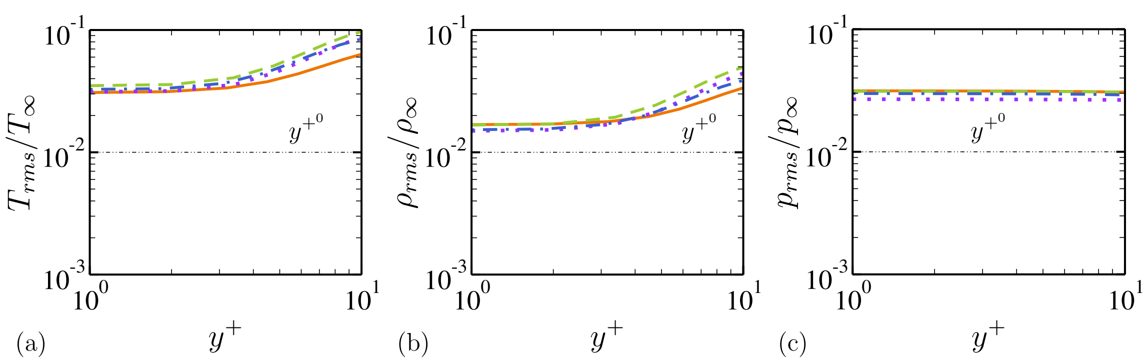

Figure 15: Near-wall asymptotic behavior of (a) the temperature, (b) the density and (c) the pressure fluctuations as a function of y^+. For legends, see table 3.

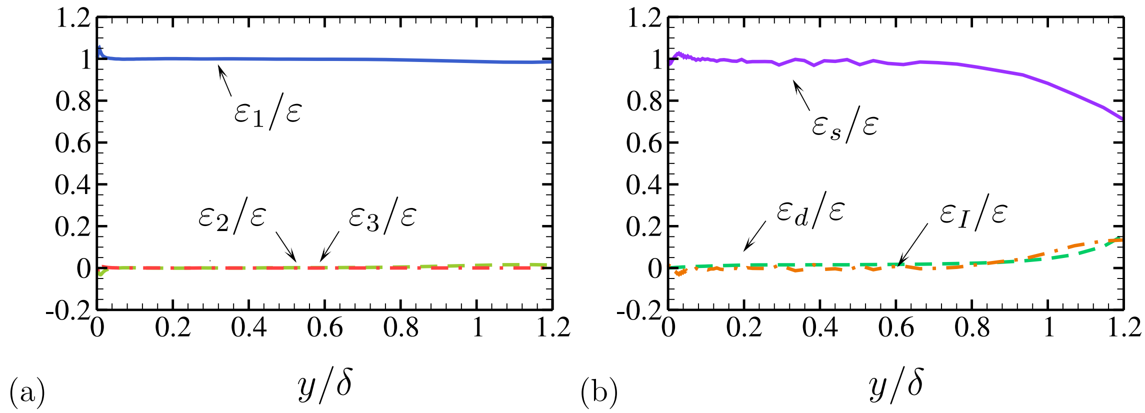

Figure 16: Ratios of the turbulent energy dissipation rate terms as a function of y/δ for CSM-M90.

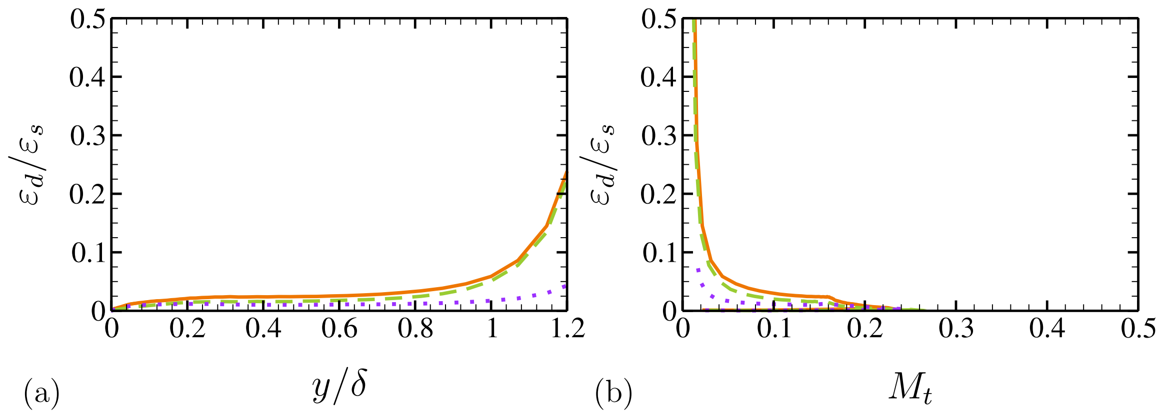

Figure 17: Ratio of the dilatational to the solenoidal dissipation as a function of (a) y/δ and (b) turbulent Mach number M_t.

Fig. (17-a) shows the ratio of dilatational dissipation to solenoidal dissipation as a function of y/δ. This ratio is found to be constant throughout the boundary layer for the WALE model, while reaching a level of 0.055 near the edge of the boundary layer for the CSM and the DSM models. Fig. (17-b) shows the ratio $\varepsilon_d/\varepsilon_s$ as a function of the turbulent Mach number. As found by Huang *et al.* (1995) [37], the relationship between $\varepsilon_d/\varepsilon_s$ and M_t is not linear. Furthermore, this result indicates that the Sarkar's [38] dilatational dissipation model, formulated for the problem of compressible shear layers growth rate, is not applicable in the case of turbulent bounded flows.

4. Conclusion

In this paper, large-eddy simulations of a spatially-evolving supersonic turbulent boundary layer over a flat plate are performed using three different SGS models. An Implicit LES (a subset of under-resolved DNS) is also investigated to assess its applicability and to see whether small truncation terms of sixth-order scheme would themselves serve as SGS models. The results are compared to both DNS and theoretical considerations and showed an overall acceptable agreement. In this study, we extend our previous work by considering high-speed compressible turbulent boundary layer for higher Re_θ and enlarged spanwise domain by a factor of two. The mesh resolution has been systematically considered to assess the effectiveness of the LES modeling compared to DNS or to well-resolved LESs. In terms of compressibility effects due to turbulent fluctuations, the LES results did confirm the early findings, in which the temperature and the velocity fluctuations are seen to be not perfectly anti-correlated, where $R_{u'T'}$ lies between 0.5 and 0.6 in a wide range of the boundary layer. Results also showed that the near wall asymptotic behavior for all relevant quantities agree very well with the DNS results for all subgrid models. The ILES is found to adhere to this observation, by predicting satisfactory results even for high-order turbulent moments. The thermodynamic fluctuations, T_{rms} and ρ_{rms}, show however a lack of independence from SGS modeling and grid refinement in contrast to the velocity fluctuating field. The pressure fluctuations, which are assumed to be associated with the acoustic mode, are not significantly affected by the modeling and the mesh resolution. By analyzing the different components of the turbulent energy dissipation rate, the present LESs show confidence to correctly predict the dissipa-tion rate. In fact, it is found that the dissipation is mainly solenoidal throughout the boundary layer, which is a classical finding for the considered case. As expected for adiabatic flows, the inhomogeneous part is negligible, due to the weak value of μ'. Also, the dilatational dissipation ε_d does not exceed 5% of the solenoidal component

ε_s within the boundary layer. As mentioned in Ben-Nasr *et al.,* (2016) [14], the cost effective choice with the CSM or the WALE model appears to be the best option when dealing with high-speed turbulent boundary layers and the acceptable quality of the ILES results did not allow us to discard unquestionably this method at least for the range of the Reynolds number we considered. Finally, it is worth mentioning that the current study has been key to develop our current level of understanding the ability of ILES and LES models to capture basic phenomena and now further LES studies of high-Reynolds number supersonic boundary layers are necessary to complete the picture. Also, further work is necessary to develop compressible formu-lation of subgrid models, especially for heated or cooled walls in presence of strong energy release due to combustion for instance, where compressibility effects are, in principle, not negligible.

Acknowledgments

This work was performed using HPC resources from GENCI [CCRT/CINES/IDRIS] (Grant 2016-0211640) and from CRIANN (*Centre Régional Informatique et d'Applications Numériques de Normandie*, Rouen. The authors acknowledge Prof. Sergio Pirozzoli, University of Rome La Sapienza, for providing his DNS data for validation.

References

[1] Chaudhuri, A., Hadjadj, A. Numerical investigations of transient nozzle flow separation. Aerospace Science and Technology, 53, 10-21 (2016).

[2] Verma, S.B., Hadjadj, A. Supersonic flow control. Shock Waves, 25, 443449 (2015).

[3] Verma, S.B., Hadjadj, A., Haidn, O. Unsteady flow conditions during dual-bell sneak transition. AIAA, Journal of Propulsion and Power, 31(4), 1175-1183 (2015).

[4] Hadjadj, A., Perrot, Y., Verma, S.B. Numerical study of shock/boundary layer interaction in supersonic overexpanded nozzles. Aerospace Science and Technology, 42, 158-168 (2015).

[5] Sow, A., Chinnayya, A., Hadjadj, A. Mean structure of one-dimensional unstable detonation with friction. Journal of Fluid Mechanics, 743, 503-533 (2014).

[6] Chinnayya, A., Hadjadj, A., Ngomo, D. Computational study of detonation-wave propagation in narrow channels. Physics of Fluids, 25, 036101 (2013).

[7] M. V. Morkovin, Effect of compressibility on turbulent flows, *Mécanique de la Turbulence, edited by A. Favre*, 1961.

[8] P. Bradshaw, Compressible turbulent shear layers, *Annu. Rev. Fluid Mech.*, 9, 33-54, 1977.

[9] A. J. Smits and J. P. Dussauge, Turbulent shear layers in supersonic flow, *American Institute of Physics, New York,* 2^{nd} *edition*, 2006.

[10] H. H. Fernholtz and P. J. Finley, A critical compilation of compressible turbulent boundary layer data, *AGARDograph*, 223 (7402), 1977.

[11] E. T. Spyropoulos and G. A. Braisdell, Large-eddy simulation of a spatially evolving supersonic turbulent boundary layer flow, *AIAA J.*, 36 (11), 1983-1990, 1998.

[12] A. Hadjadj, O. Ben-Nasr, M.S. Shadloo, A. Chaudhuri, Effect of wall temperature in supersonic turbulent boundary layers: A numerical study. *Int. J. Heat & Mass Transfer*, 81, 426–438, 2015.

[13] H. Yan, D. Knight and A. A. Zheltovodov, Large-eddy simulation of supersonic flat-plate boundary layers using the monotonically integrated large-eddy simulation MILES technique, *J. Fluids Eng.*, 124, 868-875, 2002.

[14] O. Ben-Nasr, A. Hadjadj, A. Chaudhuri and M.S. Shadloo, Assessment of subgrid-scale modeling for large-eddy simulation of a spatially-evolving compressible turbulent boundary layer, *Computers & Fluids*, (Accepted July, 2016).

[15] S. Pirozzoli, Generalized conservative approximations of split convective derivative operators. Journal of Computational Physics Volume 229, Issue 19, 20 September 2010, Pages 71807190.

[16] A. Yoshizawa, Statistical theory for compressible turbulent shear flows with the application to subgrid modeling, *Phys. Fluids*, 7, 2152-2164, 1986.

[17] P. Moin, K. Squires, W. Cabot and S. Lele, A dynamic subgrid-scale model for compressible turbulence and scalar transport, *Phys. Fluids A*, 3 (11), 2746-2757, 1991.

[18] H. Kobayashi, F. Ham and X. Wu, Application of a local SGS model based on coherent structures to complex geometries, *Int. J. Heat Fluid Flow*, 29, 640-653, 2008.

[19] H. Kobayashi, High spatial correlation SGS model for engineering turbulence, *Proceedings: 8^{th} International symposium on engineering turbulence modelling and measurements - ETMM8*, 564-596, 2010.

[20] N. Onodera, T. Aoki and H. Kobayashi, Large-eddy simulation of turbulent channel flows with conservative ISO scheme, *J. Comp. Phys.*, 230, 5787-5805, 2011.

[21] F. Nicoud and F. Ducros, Subgrid-scale stress modelling based on the square of the velocity gradient tensor, *Flow, Turbulence and Combustion*, 62, 183-200, 1999.

[22] M . Klein, A. Sadiki and J. Janicka, A digital filter based generation of inflow data for spatially developing direct numerical or large eddy simulation, *J. Comp. Phys.*, 186, 652-665, 2003.

[23] M. Bernardini and S. Pirozzoli, Wall pressure fluctuations beneath supersonic turbulent boundary layers, *Phys. Fluids*, 23 (8), 2011.

[24] S. Pirozzoli and M. Bernardini, Turbulence in supersonic boundary layers at moderate Reynolds number, *J. Fluid Mech.*, 688, 1-46, 2011.

[25] L. Duan, I. Beekman and M. P. Martin, Direct numerical simulation of hypersonic turbulent boundary layers. Part 2. Effect of wall temperature, *J. Fluid Mech.*, 655, 419-445, 2010.

[26] S. E. Guarini, R. D. Moser, K. S. Shariff and A. Wray, Direct numerical simulation of a supersonic turbulent boundary layer at Mach 2.5, *J. Fluid Mech.*, 414, 1-33, 2000.

[27] S. Pirozzoli, F. Grasso and T. B. Gatski, Direct numerical simulation and analysis of a spatially evolving supersonic turbulet boundary layer at M=2.25, *Phys. Fluids*, 16 (3), 530-545, 2004.

[28] R. Lechner, J. Sesterhenn and R. Friedrich, Turbulent supersonic channel flow, *J. Turb.*, 2, 2001.

[29] E. F. Spina, A. J. Smits and S. K. Robinson, The physics of supersonic turbulent boundary layers, *Annu. Rev. Fluid Mech.*, 26, 287-319, 1994.

[30] P. Klebanoff, Characteristics of turbulence in a boundary layer with zero pressure gradient. *Tech. rep.*, 1954.

[31] J. L. Lumley, Computational modeling of turbulent flows, *Adv. Applied Mach.*, 18, 123-176, 1978.

[32] S. B. Pope, Turbulent flows, *Cambridge Univ. Press*, 2000.

[33] P. A. Krogstad and L. E. Torbergsen, Invariant analysis of turbulent pipe flow, *Flow, Turbulence and Combustion*, 64, 161-181, 2000.

[34] M. F. Shahab, G. Lehnash, T. B. Gatski and P. Comte, Statistical characteristics of an isothermal supersonic developing boundary layer flow from DNS data, *Flow, Turbulence and Combustion*, 86, 369-397, 2011.

[35] S. Tamano, Direct Numerical Simulation of Wall-Bounded Compressible Turbulent Flow, *Nagoya Institute of Technology*, Japan, 2002.

[36] Y. Morinishi, S. Tamano and K. Nakabayashi, Direct numerical simulation of compressible turbulent channel flow between adiabatic and isothermal walls, *J. Fluid Mech.*, 502, 273-308, 2004.

[37] P. G. Huang, G. N. Coleman and P. Bradshaw, Compressible turbulent channel flows: DNS results and modeling, *J. Fluid Mech.*, 305, 185-218, 1995.

[38] S. Sarkar, G. Erlebacher M. Y. Husaini, Compressible homogeneous shear: simulation and modeling. *In turbulent shear flows*, 8, (ed. F. Durst *et al.*), Springer, 1992.